Application of Various Forward and Inverse Scattering Techniques to Non-destructive Testing (Analysis of inverse problems through partial differential equations and related topics)

AUTHOR(S):

Saitoh, Takahiro

CITATION:

Saitoh, Takahiro. Application of Various Forward and Inverse Scattering Techniques to Non-destructive Testing (Analysis of inverse problems through partial differential equations and related topics). 数理解析研究所講究録 2021, 2174: 93-107

ISSUE DATE:

2021-02

URL:

http://hdl.handle.net/2433/263959

Application of Various Forward and Inverse Scattering Techniques to Non-destructive Testing*

Takahiro Saitoh
Department of Civil and Environmental Engineering,
Gunma University[1], Japan

§1 Introduction

Over the past few decades, the Ultrasonic Non-destructive Testing (UT) has attracted attention. The objective of the UT is to identify the position, shape, and size of a defect. The ultrasonic waves satisfy the elastic wave equations in elastic materials. Consequently, numerical simulation of the ultrasonic wave propagation is reduced to solving Partial Differential Equations with initial and boundary conditions for the elastodynamics. In understanding the elastic wave propagation behavior, numerical simulation tools are useful. In general, numerical simulation tools for elastic wave propagation help obtain scattered waveforms corresponding to those at each ultrasonic transducer location in the UT experiments. The pure scattered waveforms obtained by numerical simulation tools, are used to confirm the validity of the developed inverse scattering techniques because scattered waveforms in the UT experiments normally include some signal noise. That is to say, the use of such pure scattered waveforms with no signal noise is convenient to check the validity of the developed inverse scattering formulation. For this reason, studies on the development of the inverse scattering methods to nondestructively reconstruct defects in materials had been conducted before [1][2][3][4]. The Synthetic Aperture Focusing Technique (SAFT) [1] is known as one of the defect shape reconstruction methods and is widely used because of its simple algorithm and easy implementation. In general, the SAFT base on the time-of-flight theory of the isotropic elastodynamics. Therefore, there

[1]1-5-1, Tenjin, Kiryu, Gunma, 376-8515

are only a few examples that use the SAFT for shape reconstruction of defects in anisotropic materials, including a great example by Spies et al.[2]. Kitahara et al.[4] proposed an inverse scattering technique based on the Born and Kirchhoff approximations, and applied it to type classification of defects in isotropic solids. The extension of this technique to anisotropic material had been done by Saitoh et al.[5]. However, the algorithm of the inverse scattering technique they proposed is more complicated and time-consuming than that of the SAFT. Hence, there is room for the development of new defect shape reconstruction techniques for the UT. This report presents an effort to develop a time-reversal based inverse scattering technique, which can be applied to shape reconstruction of defects in anisotropic materials. The time-reversal method was developed by Fink [6] and it uses numerical simulation tools for wave propagation. Some researches on the application of the time-reversal method to UT have been carried out in recent years, e.g., Kimoto et al.[7]. In the following section, numerical examples for the shape reconstruction of a cavity in an isotropic material are demonstrated by using a time-reversal method. The main numerical tools to simulate wave propagation are the Finite Difference Method (FDM), Finite Element Method (FEM), and Boundary Element Method (BEM). The FDM and FEM are used to analyze wave propagation in a finite and heterogeneous domain. On the other hand, the BEM can deal with an infinite region without any modifications. However, the BEM has a lot of trouble simulating the wave propagation in a heterogeneous domain. In the first example, an isotropic homogeneous infinite space is considered. Therefore, the BEM is employed for the time-reversal analysis. The second numerical example is for the position identification of a defect in an L-shaped CFRP with the anisotropic property. In this problem, the anisotropic property depends on the curved area of an L-shaped CFRP. The Voxel-based Finite Element Method (VFEM) [8] is used for handling this heterogeneous anisotropic property in the second numerical example. Applicability and validity of the time-reversal based inverse scattering method are discussed with the numerical results for these two examples.

§2 Reconstruction of cavity in isotropic and homogeneous material

In this section, the time-reversal method is applied to the reconstruction of a cavity in an isotropic and homogeneous material. The BEM has the advantage of simulating wave propagation in an infinite space, such as con-

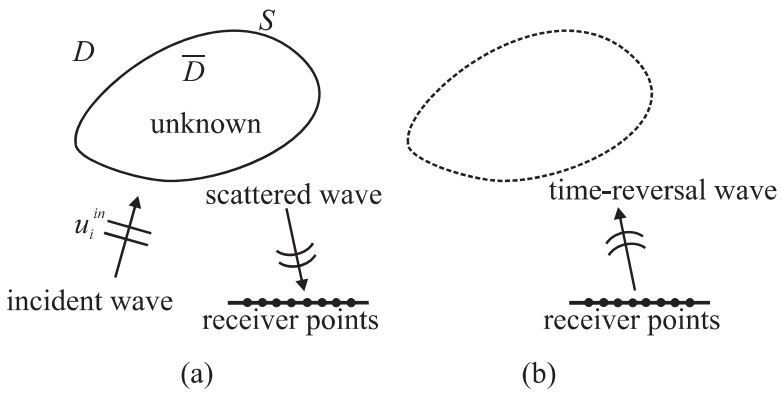

Figure 1: Elastic wave scattering by an unknown cavity in 3-D isotropic, homogeneous and infinite space.

sidered in this section. The effectiveness of the topological sensitivity for the time-reversal method is demonstrated in this section.

§2.1 Problem to be solved

Let us consider a defect shape reconstruction problem in a 3-D infinite space D as shown in Fig.1(a). Incident waves $u_i^{\rm in}(\boldsymbol{x},t)$ are scattered by an unknown cavity $\bar{D}$ with the surface S and scattered waves are received at receiver points. The displacement $u_i(\boldsymbol{x},t)$ at the position $\boldsymbol{x}$ satisfies the equation of motion and the boundary conditions as follows:

$$\begin{aligned} &\mu u_{i,jj}(\boldsymbol{x},t)+(\lambda+\mu)u_{j,ji}(\boldsymbol{x},t)=\rho\ddot{u}_i(\boldsymbol{x},t) \ \text{ in } D \\ &u_i=\bar{u}_i \ \text{ on } S_1,\ t_i=\bar{t}_i \ \text{ on } S_2, S_2=S\backslash S_1 \end{aligned} \tag{1}$$

where λ and μ are Lamé constants, t is the time, and ρ is the density of the material. $\dot{(\ )}$ and $(\ )_{,i}$ show the partial derivative $\partial/\partial t$ and $\partial/\partial x_i$, respectively. In addition, t_i is the traction component and $\bar{(\ )}$ indicates the prescribed boundary condition. Assuming the zero-initial condition, the displacement $u_i(\boldsymbol{x},t)$ satisfies the time-domain boundary integral equation as follows:

$$\begin{aligned} C_{ij}(\boldsymbol{x})u_j(\boldsymbol{x},t) &= u_i^{\rm in}(\boldsymbol{x},t) \\ &+\int_S U_{ij}(\boldsymbol{x},\boldsymbol{y},t)*t_j(\boldsymbol{y},t)dS_y-\int_S T_{ij}(\boldsymbol{x},\boldsymbol{y},t)*u_j(\boldsymbol{y},t)dS_y \end{aligned} \tag{2}$$

where C_{ij} is the free term, which depends on the boundary shape of the point $\boldsymbol{x}$ and $*$ denotes the convolution. $U_{ij}(\boldsymbol{x},\boldsymbol{y},t)$ and $T_{ij}(\boldsymbol{x},\boldsymbol{y},t)$ are the

fundamental solution and its double layer kernel for elastodynamics in time-domain. Scattered waves at the receiver points are calculated by the time-domain boundary integral equation defined by Eq. (2). The final objective of this problem is to find an unknown cavity $\bar{D}$, in the domain D, using the scattered waves obtained at the receiver points. Received waves are time-reversed and sent back into the domain D. However, the conventional time-domain BEM sometimes causes the numerical instability if we use a small time step. Therefore, in this research, the Convolution Quadrature Time-domain Boundary Element Method (CQBEM)[9][10][11] is employed to obtain scattered wave-fields and time-reversed wave-fields.

§2.2 Convolution quadrature time-domain boundary element method

In this section, the convolution quadrature time-domain boundary element formulation is briefly described. The Convolution Quadrature Method (CQM), which was first proposed by Lubich [12], approximates the convolution $f*g(t)$ by a discrete convolution using the Laplace transform of the time-dependent function $f(t-\tau)$. In general, the convolution integral is defined as follows:

$$f * g(t) = \int_0^t f(t-\tau)g(\tau)d\tau \quad , \ t \geq 0 \tag{3}$$

The convolution integral defined by Eq. (3) is approximated by CQM as follows:

$$f * g(n\triangle t) \simeq \sum_j \omega_{n-j}(\triangle t)g(j\triangle t) \tag{4}$$

where time t was divided into N equal time steps $\triangle t$. Moreover, $\omega_j(\triangle t)$ denotes the quadrature weights, which are determined by the coefficients of the following power series with complex variable z,

$$F\left(\frac{\delta(\zeta)}{\triangle t}\right) = \sum_{n=0}^{\infty} \omega_n(\triangle t)z^n \tag{5}$$

where the function F is the Laplace transform of the original time dependent function f. The power series defined in Eq.(5) can be calculated by Cauchy's integral formula. Considering a polar coordinate transformation, the Cauchy's integral is approximated by a trapezoidal rule with L equal steps, $2\pi/L$ as follows:

$$\omega_n(\triangle t) = \frac{1}{2\pi \mathrm{i}} \int_{|\zeta|=\mathcal{R}} F\left(\frac{\delta(\zeta)}{\triangle t}\right) \zeta^{-n-1} d\zeta \simeq \frac{\mathcal{R}^{-n}}{L} \sum_{l=0}^{L-1} F\left(\frac{\delta(\zeta_l)}{\triangle t}\right) e^{\frac{-2\pi \mathrm{i} n l}{L}} \tag{6}$$

where $\delta(\zeta)$ is the quotient of the generating polynomials of a linear multistep method. In addition, ζ_l is given by $\zeta_l = \mathcal{R}e^{2\pi \mathrm{i} l/L}$, $\mathcal{R}$ is the radius of a circle in the domain of analyticity of F, and i is the imaginary unit.

§2.3 Time-discretization for CQBEM

To improve the numerical stability of the conventional time-domain boundary element method, the CQM is applied to the time-discretization of the boundary integral equation defined in Eq. (2). Assuming $\boldsymbol{x} \in S$, the time-domain boundary integral equation (2) is discretized by using the CQM for time and the collocation method for space as follows:

$$\frac{1}{2}u_i(\boldsymbol{x}, n\Delta t) = u_i^{\mathrm{in}}(\boldsymbol{x}, n\Delta t) + \sum_{\alpha=1}^{M}\sum_{k=1}^{n}\left[A_{ij}^{n-k}(\boldsymbol{x}, \boldsymbol{y}^\alpha)t_j^\alpha(k\Delta t) - B_{ij}^{n-k}(\boldsymbol{x}, \boldsymbol{y}^\alpha)u_j^\alpha(k\Delta t)\right] \quad (7)$$

where A_i^m and B_i^m are the influence functions defined by

$$A_{ij}^m(\boldsymbol{x}, \boldsymbol{y}) = \frac{\mathcal{R}^{-m}}{L}\sum_{l=0}^{L-1}\int_S \hat{U}_{ij}(\boldsymbol{x}, \boldsymbol{y}, s_l)e^{-\frac{2\pi \mathrm{i} m l}{L}}dS_y \quad (8)$$

$$B_{ij}^m(\boldsymbol{x}, \boldsymbol{y}) = \frac{\mathcal{R}^{-m}}{L}\sum_{l=0}^{L-1}\int_S \hat{T}_{ij}(\boldsymbol{x}, \boldsymbol{y}, s_l)e^{-\frac{2\pi \mathrm{i} m l}{L}}dS_y \quad (9)$$

where s_l is given by $s_l = \delta(\zeta_l)/(\triangle t)$. The parameter $\mathcal{R}$ has the condition: $\mathcal{R} < 1$ and is taken as $\mathcal{R}^L = \sqrt{\epsilon}$ where ϵ shows the assumed error in the calculation of Eqs.(8) and (9). $\hat{U}_{ij}(\boldsymbol{x}, \boldsymbol{y}, s)$ is the Laplace domain fundamental solution for 3-D elastodynamics as follows:

$$\hat{U}_{ik}(\boldsymbol{x}, \boldsymbol{y}, s) = \frac{1}{4\pi\mu}\left\{\frac{e^{-s_T r}}{r}\delta_{ik} - \frac{1}{s_T^2}\frac{\partial^2}{\partial y_i \partial y_k}\left(\frac{e^{-s_T r}}{r} - \frac{e^{-s_L r}}{r}\right)\right\} \quad (10)$$

where s_β is defined by $s_\beta = s/c_\beta, (\beta = L \text{ or T})$, and c_L and c_T are the wave velocities of longitudinal and transverse waves, respectively. In addition, r is given by $r = |\boldsymbol{x} - \boldsymbol{y}|$ and δ_{ik} is the Kronecker delta. The traction fundamental solution $\hat{T}_{jk}(\boldsymbol{x}, \boldsymbol{y}, s)$ is calculated by

$$\hat{T}_{jk}(\boldsymbol{x}, \boldsymbol{y}, s) = n_i(\boldsymbol{x})\Sigma_{ijk}(\boldsymbol{x}, \boldsymbol{y}, s) \quad (11)$$

where Σ_{ijk} is the traction operator[13] and $n_i(\boldsymbol{x})$ is the component of an outward unit normal vector with respect to $\boldsymbol{x}$. $\delta(\zeta_l)$ is calculated by $\delta(\zeta_l) =$

$(1-\zeta_l)+(1-\zeta_l^2)/2$. Eqs. (8) and (9) are identical to the discrete Fourier transform. Therefore, the calculations of Eqs. (8) and (9) can be evaluated by means of the fast Fourier transform. Eq. (7) can be rewritten according to the boundary conditions as follows:

$$\begin{aligned}&\frac{1}{2}u_i(\boldsymbol{x},n\triangle t)+\sum_{\alpha=1}^{M}\left[B_{ij}^0(\boldsymbol{x},\boldsymbol{y}^\alpha)u_j^\alpha(n\triangle t)-A_{ij}^0(\boldsymbol{x},\boldsymbol{y}^\alpha)t_j^\alpha(n\triangle t)\right]\\ =&u_i^{\text{in}}(\boldsymbol{x},n\triangle t)+\sum_{\alpha=1}^{M}\sum_{k=1}^{n-1}\left[A_{ij}^{n-k}(\boldsymbol{x},\boldsymbol{y}^\alpha)t_j^\alpha(k\triangle t)-B_{ij}^{n-k}(\boldsymbol{x},\boldsymbol{y}^\alpha)u_j^\alpha(k\triangle t)\right].\end{aligned} \tag{12}$$

For the n-th time step, all the quantities on the right-hand side of Eq. (12) are known. Therefore, the unknown values u_i^α and t_i^α at the n-th time step can be obtained by solving Eq. (12).

§2.4 Topological sensitivity for 3-D isotropic elastodynamics

An unknown cavity $\bar{D}$, in the domain D, is reconstructed using the time-reversal method. Scattered waves observed at receiver points are time-reversed and their time-reversed waves are transmitted back into the domain D, as the incident waves from receiver points. The time-reversed wave-fields are calculated using the boundary integral equation defined in Eq. (2). The time-reversed waves are going back to the scattering source, which is the surface S, of a cavity $\bar{D}$. The unknown cavity position is determined by the focusing point of the time-reversed waves. In this study, the topological sensitivity $\mathcal{T}(\boldsymbol{x})$ for 3-D elastodynamics proposed by Bonnet [14] is introduced to determine the focusing point of the time-reversal waves:

$$\mathcal{T}(\boldsymbol{x})=\left\{\nabla\tilde{\boldsymbol{u}}*(\boldsymbol{A}:\nabla\boldsymbol{u})+\rho\dot{\boldsymbol{u}}*\dot{\tilde{\boldsymbol{u}}}\right\}(\boldsymbol{x},T) \tag{13}$$

where $\tilde{\boldsymbol{u}}$ shows the time-reversal wave fields. The component of $\boldsymbol{A}$ is given by

$$A_{ijkl}=\frac{3(1-\nu)}{2(1+\nu)(7-5\nu)}\left\{\frac{-(1-14\nu+15\nu^2)E}{(1-2\nu)^2}\delta_{ij}\delta_{kl}+5E(\delta_{ik}\delta_{jl}+\delta_{il}\delta_{jk})\right\} \tag{14}$$

where ν and E are Poisson's ratio and Young modulus, respectively. The topological sensitivity $\mathcal{T}(\boldsymbol{x})$ in Eq. (13) allows us to quantify the sensitivity

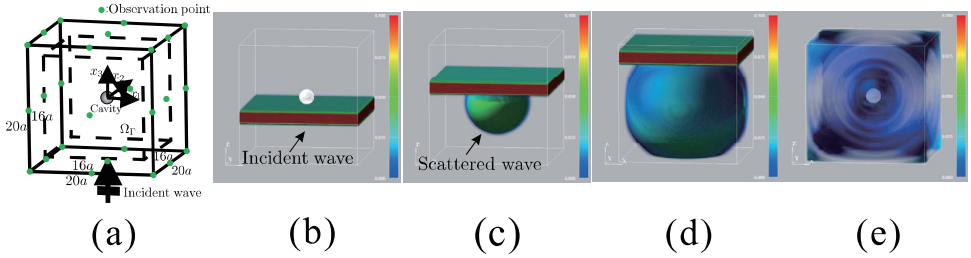

Figure 2: Elastic wave scattering by a cavity in 3-D homogeneous and isotropic space (a) analysis model (b) total wave-field $|\boldsymbol{u}|$ at $c_L t/a = 0.02768$ (c) at $|\boldsymbol{u}|$ at 3.8752 (d) at $c_L t/a$=8.0272 (e) at $c_L t/a$=23.528.

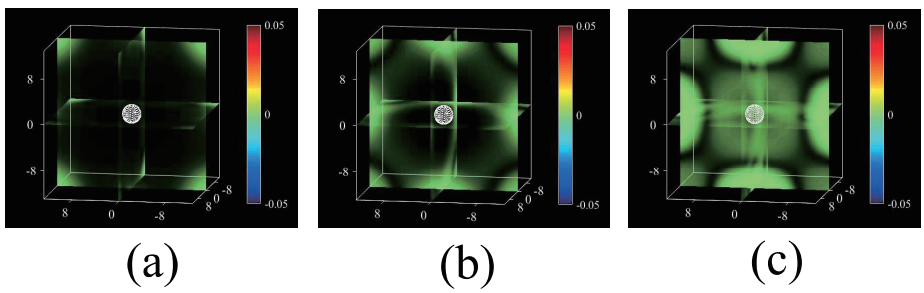

Figure 3: Time-reversal wave field at (a) $c_L t/a = 1.384$ (b) $c_L t/a = 2.491$ (c) $c_L t/a = 3.322$.

of a problem when the domain under consideration is perturbed by the introduction of an infinitesimal hole. Considering a cavity as the superposition of infinitesimal holes, the topological sensitivity may help to identify the cavity position if we assume the defect as the cavity. The existence of an unknown cavity shows smaller negative values of the topological sensitivity $\mathcal{T}(\boldsymbol{x})$ in the domain D. Therefore, an unknown cavity position can be determined by using this fact. The detail of the topological sensitivity for 3-D elastodynamics can be seen in the paper [14]. See [15] for more details of the numerical procedure for the cavity position determination process.

§2.5 Numerical examples for shape reconstruction of cavity in isotropic material using time-reversal method

The time-reversal method is applied to the shape reconstruction of a single cavity with the radius a, in an infinite elastic solid, as shown in Fig. 2(a).

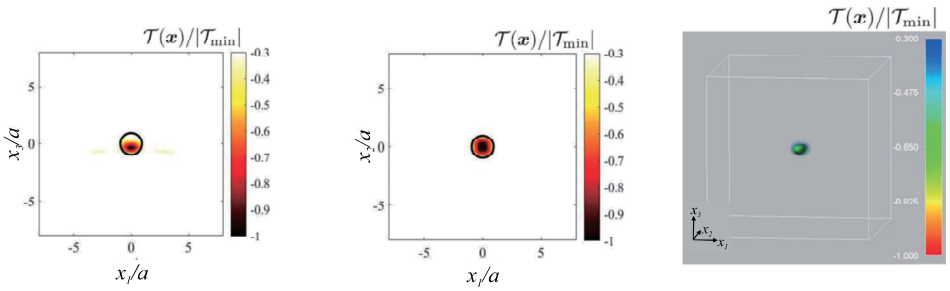

Figure 4: Distribution of the topological sensitivity $\mathcal{T}(\boldsymbol{x})$ on (a) x_1-x_3 plane (b) x_1-x_3 plane, and (c) in a 3-D view.

The topological sensitivity $\mathcal{T}(\boldsymbol{x})$ defined in Eq.(13) is utilized to determine the cavity position. Figures 2(b)-(e) show the total elastic wave fields around the cavity at several time steps. The following incident plane wave $u_i^{\text{in}}(\boldsymbol{x}, t)$ with the amplitude u_0 traveling in the upward direction (x_3 direction) is considered:

$$u_i^{\text{in}}(\boldsymbol{x}, t) = u_0 \left(1 - \cos\Theta\right), \quad 0 \le \Theta = t - \frac{x_3 + a}{c_L} \le 2\pi, \text{ otherwise } \Theta = 0 \tag{15}$$

The parameters are taken as $N = L = 1024$ in Eqs. (8) and (9), and $c_L \Delta t/a = 0.02768$. The spherical cavity is discretized into the 384 boundary elements. The incident wave $u_i^{\text{in}}(\boldsymbol{x}, t)$ hits the cavity as shown in Fig. 2(b), and the scattered waves are generated by the interaction between the cavity surface and the incident plane wave coming from the bottom. In addition, scattered waves are propagating to the infinite distance, as shown in Figs. 2(b)-(e). These scattered waves are received at the 27 observation points, which are shown by the green points on the cube centered on the origin, with a side length of $40a$, drawn with a solid line in Fig. 2(a). The received scattered waves are time-reversed and sent back into the domain from the 27 observation points. Figures 3(a)-(c) show the time-reversed wave-fields at various time steps in a 3-D view. The real cavity located at the center in Figs. 3(a)-(c) is not considered in this time-reversal analysis. As shown in Figs. 3(a)-(c), the time-reversed waves are transmitted at the time, $c_L t/a = 0.0$, then, propagating, and approaching to the cavity. These time-reversed and the scattered wave-fields, as shown in Fig. 2 and Fig. 3, respectively, are used to calculate the topological sensitivity $\mathcal{T}(\boldsymbol{x})$ in Eq. (13). Figures 4(a) and (b) show the distribution of the topological sensitivity $\mathcal{T}(\boldsymbol{x})$ on x_1-x_3 plane and x_1-x_2 plane, respectively. The black solid circle in Figs.4(a) and (b) indicates the real cavity. On the other hand, Fig. 4(c) shows the same

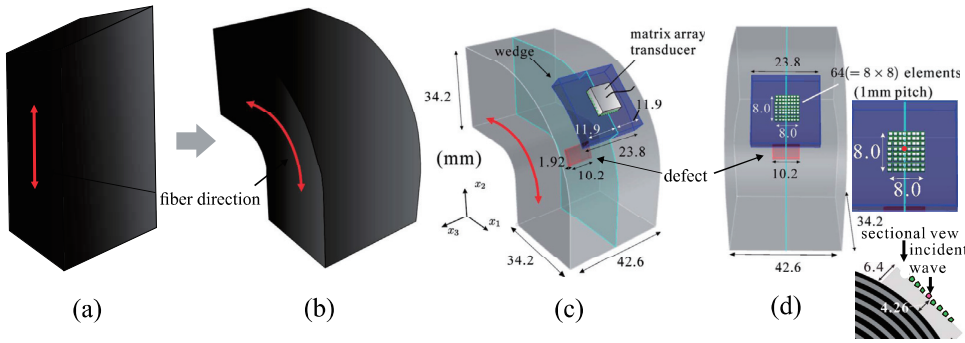

Figure 5: Schematic of an L-shaped CFRP (a) bent uni-directional CFRP (b) its transparent view (c) view from x_1 direction.

result but in a 3-D view. In Fig. 4(a), the upper side of the cavity is not reconstructed accurately. This is due to the fact that the incident plane wave $u_i^{\text{in}}(\boldsymbol{x}, t)$ defined in Eq. (15) travels to the positive x_3 direction and directly hits the lower side of the cavity. However, the cavity position and shape are generally reconstructed as shown in Figs.4(b) and (c). Therefore, the time-reversal technique with the topological sensitivity is effective for the defect position detection in the UT.

§3 Reconstruction of defect in L-shaped CFRP

In this section, the defect shape reconstruction for L-shaped CFRP is considered. In general, CFRPs have the anisotropic property, which complicates the understanding of the elastic wave propagation behavior in CFRPs. Unfortunately, the BEM has trouble in solving anisotropic elastodynamic problems because the fundamental solutions for anisotropic elastodynamic problems cannot be obtained in the closed form [16]. The computation for the non-closed form of fundamental solutions is very time-consuming. In addition, complicated CFRPs, such as L-shaped and T-shaped CFRPs, indicate the property of inhomogeneous anisotropy. The BEM has difficulty in dealing with an inhomogeneous domain without any modifications, whose material property varies arbitrarily. Therefore, in this study, the FEM is selected as a technique to simulate wave propagation and scattering. In this section, the primary focus of the study is to consider the applicability of the time-reversal method to the defect shape reconstruction for an L-shaped CFRP with inhomogeneous and anisotropic properties.

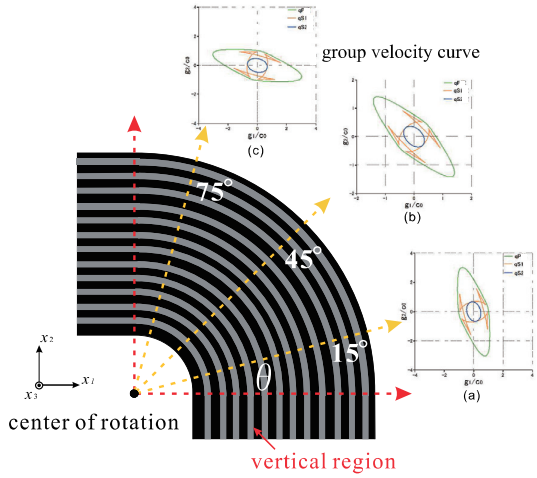

Figure 6: Group velocity curves in the curbed area of Fig. 5(b)-(d).

§3.1 L-shaped CFRP model

Let us consider elastic wave scattering by a defect in an L-shaped CFRP, as shown in Fig. 5(b). The L-shaped CFRP is made by bending a straight unidirectional CFRP in a longitudinal direction, which is the consistent with x_2 direction, as shown in Fig. 5. An ultrasonic matrix array transducer with a wedge is used to detect the defect of the L-shaped CFRP. The anisotropic property depends on the orientation of the carbon fiber, which is shown by the red curved line with a double-headed arrow in Figs. 5(a) and (b). It is assumed that the elastic constants continuously vary in the curved area, as shown in Fig. 5(b). The elastic wave-fields by a defect in the L-shaped CFRP are calculated by the FEM. The scattered waves generated by the interaction between the transmitted waves from the matrix array transducer and defect are received by the array transducers, and the received waves at the elements of the matrix array transducer are re-transmitted into the L-shaped area in order to identify the position of the defect using the time-reversal method. The VFEM used in this analysis is well known. Therefore, the detail of the VFEM formulation is skipped in this report.

§3.2 Group velocity curve

Three types of bulk waves: qP, qS1, and qS2, exist in anisotropic materials. The behaviors of these three types of waves are confirmed before showing numerical results. In general, the group velocity curve [17] is useful to check the wave front of these three waves. The group velocity curve is derived from

solving the Christoffel equation. The group velocity curve can be drawn using the elastic constants of a target material. In this analysis, the elastic constants $C_{\alpha\beta}(\alpha, \beta = 1, \ldots, 6)$ of the original straight CFRP in Fig.5(a) before being bent are assumed in Voigt notation as follows:

$$C_{\alpha\beta} = \begin{bmatrix} 16.3 & 3.72 & 4.96 & 0 & 0 & 0 \\ & 155.4 & 3.72 & 0 & 0 & 0 \\ & & 16.3 & 0 & 0 & 0 \\ & & & 7.48 & 0 & 0 \\ & \text{sym.} & & & 3.37 & 0 \\ & & & & & 7.48 \end{bmatrix} \text{[GPa]} \tag{16}$$

In Fig. 5(a), the fiber direction is consistent with the x_2 direction. Therefore, C_{22} has a larger value than the other components of $C_{\alpha\beta}$. Figure 6 shows the x_1-x_2 cross-section of the analysis model. The elastic constant, C, expressed in Eq. (16) is used for the vertical region in Fig. 6. On the other hand, the elastic constant, C', for each part of the L-shaped area is calculated using the angle θ on the center of ration in Fig. 6 as follows [18][19]:

$$C' = KCK^T \tag{17}$$

where K is the coordinate system transformation matrix, and K^T is the transpose of K. The anisotropic principle axis is taken along to the fiber direction of Fig. 6, which is drawn by the gray curved lines. The transformation matrix, K, is calculated by taking into account the anisotropic principle axis transformation according to the fiber direction. The group velocity curves for $\theta = 15°, 45°$, and $75°$ in the x_1-x_2 plane are also shown in Fig. 6, which are normalized by $c_0 = \sqrt{C_{66}/\rho}$, and ρ is set as $\rho = 1600$ kg/m^3. Each wave-front for qP, qS1, and qS2 waves is drawn by green, red, and blue lines, respectively, in these group velocity curves. As understood in these group velocity curves, qP wave is the fastest and propagates according to the fiber direction.

§3.3 Numerical examples for reconstruction of defect in L-shaped CFRP using time-reversal method

A numerical example for the reconstruction of the defect in Figs. 5(c) and (d) is demonstrated in this section. The density, ρ, and the elastic constant, C, mentioned in the previous section 3.2 are used in this analysis. The incident wave period T is given by $T = 1/f_p = 2.0 \times 10^{-6}$(s). Figure 7 shows total wave-fields, $|\boldsymbol{u}|$, around the defect in the L-shaped CFRP obtained by the FEM with the time increment, $\Delta t = 1.0 \times 10^{-8}$(s). A matrix array

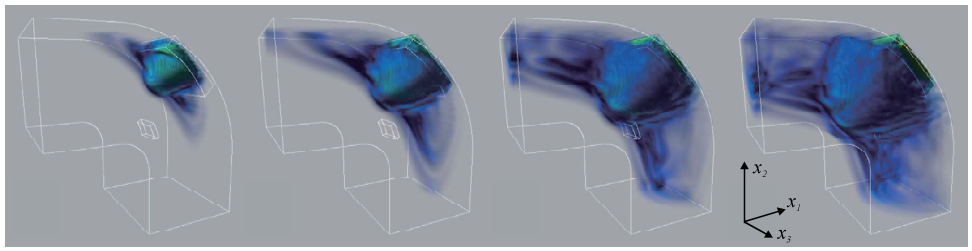

Figure 7: Total displacement fields in the L-shaped CFRP of Fig. 5(b) at times (a) $600\Delta t$ (b) $800\Delta t$ (c) $1000\Delta t$ and (d) $1200\Delta t$.

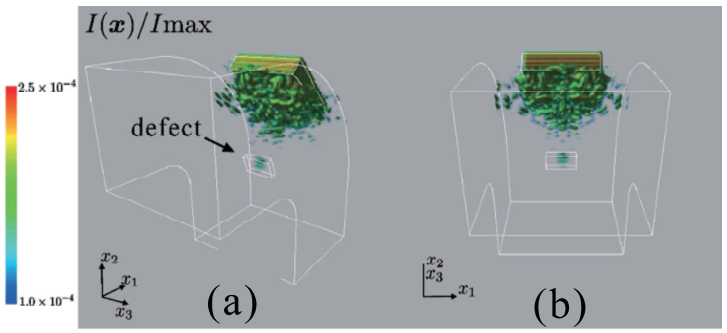

Figure 8: Cross-spectrum distributions in CFRP (a) a three-quarter view (b) x_3 direction view.

transducer, with $8\times 8 = 64$ elements, is considered, and the incident spherical wave is transmitted from one element of the transducer, shown by the red point through the intermediary of the wedge, as shown in Fig. 5(d). In this analysis, the Ricker-wavelet is assumed as the incident wave and the displacement is given at the incident red point, as shown in Fig. 5(d), as follows:

$$\boldsymbol{u}^{\text{in}} = \boldsymbol{u}_0 \frac{\sqrt{\pi}}{2}\Big(\alpha - 0.5\Big)\exp(-\alpha), \alpha = \Big[\Big(\frac{\pi(t-t_s)}{t_p}\Big)\Big]^2 \tag{18}$$

where $\boldsymbol{u_0}$, t_p and t_s are given as $\boldsymbol{u_0} = (1,1,0)$, $t_p = 500$kHz and $t_s = 1/f_p$, respectively. It can be confirmed that the qP wave propagates according to the carbon fiber direction with the fastest speed. Scattered waves generated by the defect in the L-shaped CFRP are received by the matrix array transducer, time-reversed, and sent back into the L-shaped CFRP. In the previous section, the topological sensitivity was utilized to identify the defect position. However, Eqs. (13) and (14) can be applied to obtain $\mathcal{T}(\boldsymbol{x})$ in isotropic elas-

tic solids. Therefore, in this section, the cross-spectrum calculated by the time-reversal waves and the incident waves, whose details are skipped due to the page limitation is used for the defect position identification for the L-shaped CFRP with the anisotropic property[19][20]. Figure 8 indicates the distribution of the cross-spectrum calculated by the time-reversed waves and the incident waves and each of Fig. 8(a) and (b) shows the distribution seen from a three-quarter and x_3 direction view, respectively. In Fig. 8, the cross-spectrum shows a large value in the vicinity of the defect. The time-reversal method using the cross-spectrum can correctly identify the defect position. However, the cross-spectrum also indicates the large value exactly below the wedge. This fact might be caused by the multiple scattering between the wedge and the L-shape CFRP but it is still unclear. It is concluded that the time-reversal method using the cross-spectrum is effective to identify the defect position in not only isotropic, but also in anisotropic materials such as the L-shaped CFRP shown in this report.

§4 Conclusions

In this report, the application of time-reversal methods to the UT is considered. The shape reconstruction of a cavity in 3-D infinite, isotropic, and homogeneous solid is considered using the time-reversal method where the topological sensitivity was employed to identify a cavity. On the other hand, in order to identify the position of the defect in the L-shaped CFRP, the cross-spectrum is considered. In spite of the strong anisotropic property of the L-shaped CFRP, the defect position identification is established. These numerical results show the potential of the application of time-reversal methods to practical UT applications. The time-reversal method is one of the elegant ways for defect detection in the UT. However, the calculations for the topological sensitivity and the cross-spectrum need the wave-fields data inside the test materials. This is a demerit because only the received waves on the surface of the test materials are obtained by transducers on-site UT and the wave-field data within the test materials cannot be obtained. Therefore, the time-reversal method may be useful for a digital twin UT, which is a virtual UT using Information and Communication Technology environment, and the computational mechanics.

Acknowledgment

This work was supported by "JSPS KAKENHI (17H03294)", "Joint Usage/Research Center for Interdisciplinary Large-scale Information Infrastructures", and "High Performance Computing Infrastructure" in Japan (Project ID: jh190073-NAH and jh200052-NAH). Tha author gives thanks to H. Morikawa, Y. Maehara and M. Tashiro, who are master students of Gunma University, for their kind support.

References

[1] S. R. Doctor, T. E. Hall, and L. D. Reid : Saft - the evolution of a signal processing technology for ultrasound testing, *NDT Int.*, **19**(3) (1986), pp.163-167.

[2] M. Spies and W. Jager : Synthetic aperture focusing for defect reconstruction in anisotropic media, *Ultrasonics*, **41**(2) (2003), pp.125-131.

[3] D. Colton, J. Coyle and P. Monk : Recent developments in inverse acoustic scattering theory, *SIAM Review*, **42**(3) (2000), pp.369-414.

[4] M. Kitahara, K. Nakahata and S. Hirose : Elastodynamic inversion for shape reconstruction and type classification of flaws, *Wave Motion*, **36** (2002), pp.443-455.

[5] T. Saitoh, Y. Inagaki and M. Shimoda: 2-D inverse scattering analysis for a defect in anisotropic solids *J. JSNDI*, **66**(2) (2017), pp.84-89 (in Japanese).

[6] M. Fink: Time reversal of ultrasonic fields - PartI: Basic principles, *IEEE. T. Ultrason Ferr*, **39**(5) (1992), pp.555-566.

[7] K. Kimoto, K. Nakahata and T. Saitoh: An elastodynamic computational time-reversal method for shape reconstruction of traction-free scatterers, *Wave Motion*, **72** (2017), pp.23-40.

[8] K. Terada, T. Miura and N. Kikuchi: Digital image-based modeling applied to the homogenization analysis of composite materials, *Comput. Mech.*, **20**(4) (1997), pp.331-346.

[9] M. Schanz and H. Antes: Application of operational quadrature methods in time domain boundary element method, *Meccanica*, **32** (1997), pp. 179-186.

[10] A. I. Abreu, J. A. M. Carrer and W. J. Mansur: Scalar wave propagation in 2D: a BEM formulation based on the operational quadrature method, *Eng. Anal. Bound. Elem.*, **27** (2003), pp. 101-105.

[11] T. Saitoh, S. Hirose and T. Fukui: Convolution quadrature boundary element method and acceleration by fast multipole method in 2-D viscoelastic wave propagation, *Theor. Appl. Mech. Japan*, **57** (2009), pp. 385-393.

[12] C. Lubich: Convolution quadrature and discretized operational calculus I, *Numer. Math.*, **52** (1988), pp.129-145.

[13] S. Kobayashi, T. Fukui, M. Kitahara, N. Nishimura and S. Hirose: Wave analysis and boundary elements, Kyoto University Press (2000) (in Japanese).

[14] M. Bonnet: Topological sensitivity for 3D elastodynamic and acoustic inverse scattering in the time domain, *Comput. Method Appl. M.*, **195** (2014), pp.5239-5254.

[15] H. Morikawa, T. Saitoh and K. Kimoto: Application of time-reversal method using topological sensitivity for defect detection to ultrasonic phased array testing, *J. Japan Society of Civil Eng.*, Ser. A2 (Applied Mechanics (AM)), **74**(2) (2018), pp. I_85-I_93 (in Japanese).

[16] A. Furukawa, T. Saitoh and S. Hirose: Convolution quadrature time-domain boundary element method for 2-D and 3-D elastodynamic analyses in general anisotropic elastic solids, *Eng. Anal. Bound. Elem.*, **39** (2014), pp.64-74.

[17] B. A. Auld: Acoustic fields and waves in solids, vol. 1,2, (1990), R. E. Krieger.

[18] Y. Maehara and T. Saitoh: Shape reconstruction of a defect in L-shaped CFRP using time-reversal method, *J. JASCOME*, **18** (2018), pp.47-52 (in Japanese).

[19] Y. Maehara and T. Saitoh: 3-D forward and time-reversal analysis for defect in bent CFRP using finite element method, *J. JASCOME*, **19** (2019), pp.103-108 (in Japanese).

[20] K. Nakahata, Y. Amano, H. Mizota, T. Saitoh and K. Kimoto: Construction of numerical model using wavefield data and its application of flaw imaging by time reversal method, *J. Japan Society of Civil Eng.*, Ser. A2 (Applied Mechanics (AM)), **75**(2) (2019), pp. I_71-I_81 (in Japanese).